EDGE ARTICLE

Insights into the structure–photoreactivity relationships in well-defined perovskite ferroelectric KNbO₃ nanowires†

Tingting Zhang,[ab] Wanying Lei,[a] Ping Liu,[c] José A. Rodriguez,[c] Jiaguo Yu,[d] Yang Qi,[b] Gang Liu*[a] and Minghua Liu*[a]

Structure–function correlations are a central theme in heterogeneous (photo)catalysis. In this study, the geometric and electronic structure of perovskite ferroelectric KNbO₃ nanowires with respective orthorhombic and monoclinic polymorphs have been systematically addressed. By virtue of aberration-corrected scanning transmission electron microscopy, we directly visualize surface photocatalytic active sites, measure local atomic displacements at an accuracy of several picometers, and quantify ferroelectric polarization combined with first-principles calculations. The photoreactivity of the as-prepared KNbO₃ nanowires is assessed toward aqueous rhodamine B degradation under UV light. A synergy between the ferroelectric polarization and electronic structure in photoreactivity enhancement is uncovered, which accounts for the prominent reactivity order: orthorhombic > monoclinic. Additionally, by identifying new photocatalytic products, rhodamine B degradation pathways involving N-deethylation and conjugated structure cleavage are proposed. Our findings not only provide new insights into the structure–photoreactivity relationships in perovskite ferroelectric photocatalysts, but also have broad implications in perovskite-based water splitting and photovoltaics, among others.

Introduction

Since Fujishima and Honda discovered photocatalytic water splitting on TiO₂,[1] the past decades have seen a significant rise in light-driven pollutant abatement,[2–5] selective oxidation,[6,7] and water splitting.[8–14] Despite tremendous progress being made, the mechanisms of photocatalysis are not yet known in detail. In the conceptual framework of heterogeneous (photo)catalysis, the mechanistic understanding of structure–function relationships is a prerequisite to the rational design of efficient photocatalysts. On the other hand, semiconductor-based photocatalysis is inherently complex in that both the surface structure and bulk structure of a given photocatalyst synergistically dictate the photocatalytic efficiency:[5,15] the bulk absorbs incident photons and generates e⁻–h⁺ pairs, while the surface

harnesses available e⁻–h⁺ to catalyze target adsorbates at the photocatalytic active sites. To this end, a driving force (*e.g.*, internal electronic field functional like a p–n junction) for facilitating the spatial separation of the e⁻–h⁺ pairs is desirable.[16–21] Apparently, the complexity of photocatalysis hampers an atomistic understanding of structure–function relationships. For instance, most previous studies about internal electronic field-mediated photocatalysis are carried out on irregularly-shaped powders in which the active sites are unclear,[22–24] making it difficult to explore structure–function relationships. Only a thorough understanding of structure–function relationships in well-defined model catalysts can add new dimensions to our fundamental view of "real world" catalysis as well as rationally design catalysts at an atomic-level.[25–27] Recent advances in synthesizing nanocrystals allow for fine control of the size and shape of (photo)catalysts.[28–31] To date, a great deal of studies on nanostructured photocatalysts are focused on facet-dependent photocatalysis.[32–38] Nevertheless, the underlying synergetic effects involved in photocatalysis remain largely unexplored.

In this study, we investigated the photocatalytic degradation of rhodamine B (RhB) in water (a model reaction in the removal of organic pollutants from waste water) by one-dimensional (1D) single-crystalline potassium niobate (KNbO₃) nanowires (NWs) with respective orthorhombic and monoclinic polymorphs. KNbO₃ is a typical ferroelectric perovskite (general formula ABO₃, where A is a metal, B is a second metal, and O is

aNational Center for Nanoscience and Technology, Beijing 100190, China. E-mail: liug@nanoctr.cn; liuminghua@nanoctr.cn

bInstitute of Materials Physics and Chemistry, School of Sciences, Northeastern University, Shenyang 110004, China

cChemistry Department, Brookhaven National Laboratory, Upton, New York 11973, USA

dState Key Laboratory of Advance Technology for Material Synthesis and Processing, Wuhan University of Technology, Wuhan 430070, China

oxygen) with diverse emerging technological applications, including photocatalysis, with the advantages of non-toxicity, cost-effectiveness and high stability under light illumination.[39,40] In 1D nanostructures, it is possible to enhance the photoreactivity by tuning the transport of photogenerated charge carriers through quantum confinement.[41,42] Currently, the understanding of ferroelectric materials is based primarily on theory, since few experimental techniques can be used to probe the local atomic displacements that give rise to polarization. Thanks to recent progress in aberration-corrected transmission electron microscopy (TEM),[43,44] it is possible to measure local polarization displacements at an accuracy of several picometers and determine surface terminations by profile imaging. Herein, using advanced aberration-corrected scanning transmission electron microscopy (STEM), we directly visualize surface photocatalytic active sites, measure local atomic displacements at an accuracy of several picometers, and quantify ferroelectric polarization combined with spin-polarized density functional theory (DFT) calculations. We uncover a novel photocatalytic synergy between ferroelectric polarization and electronic structure, which accounts for the prominent reactivity order: orthorhombic > monoclinic. Additionally, RhB degradation pathways involving N-deethylation and conjugated structure cleavage are proposed.

Results and discussion

Fig. 1a and b illustrate the crystal structures of monoclinic and orthorhombic KNbO$_3$ polymorphs, denoted as m-KNbO$_3$ and o-KNbO$_3$, respectively. X-ray diffraction (XRD) patterns as displayed in Fig. 1c confirm the as-prepared m-KNbO$_3$ (space group $P1m1$) and o-KNbO$_3$ (space group $Bmm2$, JCPDS card 71-2171) samples with comparable crystallinity, evidenced by the full-width at half-maximum (FWHM), $e.g.$, about 0.23° for the peak at 31.5° for m-KNbO$_3$ and o-KNbO$_3$. High-resolution XRD in the

range of 44°–46° (Fig. 1d) further indicates apparent structural differences between the above two structures. Scanning electron microscopy (SEM) images (Fig. 1e and f) show well-defined elongated m- and o-KNbO$_3$ NWs. Combined SEM and atomic force microscopy (AFM) (Fig. S1†) measurements indicate that the average length, width, and height for the m-KNbO$_3$ NWs are (1.3 ± 0.5) μm, (106 ± 47) nm, and (138 ± 36) nm, respectively, while for the o-KNbO$_3$ NWs they are (1.2 ± 0.4) μm, (102 ± 27) nm, and (136 ± 17) nm, respectively. High-resolution transmission electron microscopy (HRTEM) images (Fig. S2†) prove that the m-KNbO$_3$ NWs are enclosed by {100}, {010} and {001} facets,[45] and the o-KNbO$_3$ NWs are enclosed by {101} and {010} facets.[46] The growth direction of the m- and o-KNbO$_3$ NWs is [100] and [101], respectively. The BET specific surface area is measured to be 4.7 and 4.8 m^2 g^{-1} for the respective m- and o-KNbO$_3$ NWs.

The photophysical property is revealed by diffuse-reflectance UV-vis (DRUV-vis) spectroscopy (Fig. 2a). The bandgap (E_g) of the KNbO$_3$ NWs is determined using a Tauc plot (in the inset of Fig. 2a): the m- and o-KNbO$_3$ NWs possess a bandgap of 3.15 and 3.25 eV, respectively. The bandgap of o-KNbO$_3$ is similar to that reported in previous work (3.2 eV).[47] Peak A centered at 531.4 eV is ascribed to the hybridization of O 2p with Nb 4d–t$_{2g}$ through π* interaction. Both peaks B and C, observed at 535.0 and 537.8 eV respectively, are attributed to the hybridization of O 2p with Nb 4d–e$_g$ (σ* interaction) and Nb 5p (π*, σ* interaction).[48] The relative peak intensity ratio between A and C is dramatically decreased from m- to o-KNbO$_3$ NWs, suggesting that the O chemical environment is different in the m- and o-KNbO$_3$ NWs. High-resolution X-ray photoelectron spectroscopy (XPS) spectra (Fig. 2c) indicate that Nb 3d$_{5/2}$ is $ca.$ 206.5 and 206.6 eV for m- and o-KNbO$_3$ NWs, respectively. Fig. 2d reveals that the m- and o-KNbO$_3$ NWs present similar valence band (VB) maxima ($ca.$ 2.2 eV) and line shape, and no detectable oxygen vacancy defects exist. Since the o-KNbO$_3$ NWs have a greater
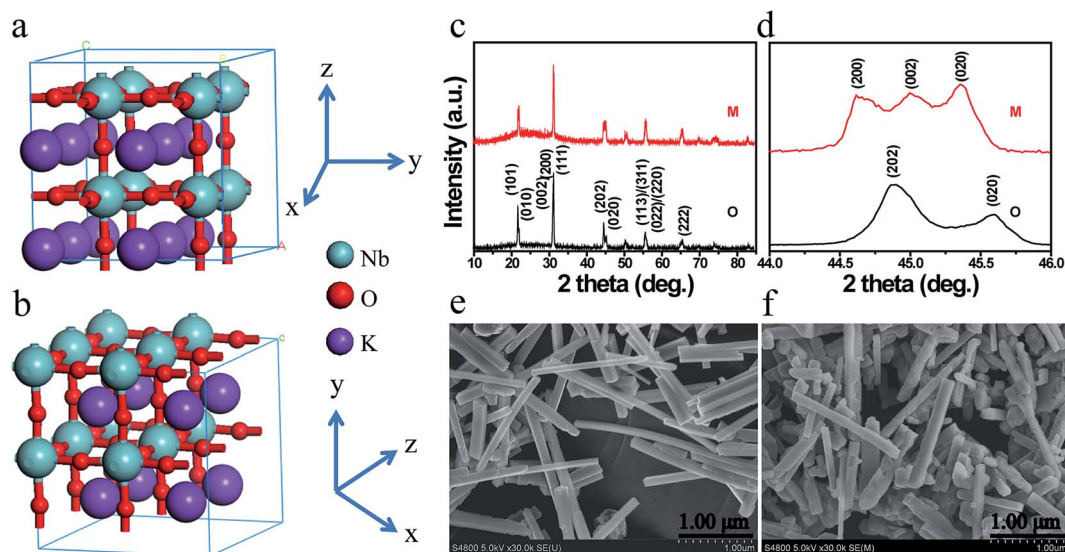
Fig. 1 (a) Crystal structure of m-KNbO$_3$. (b) Crystal structure of o-KNbO$_3$. (c) Powder XRD patterns of m- and o-KNbO$_3$ NWs. (d) High-resolution XRD patterns in the range of 44°–46°. (e) SEM image of m-KNbO$_3$ NWs. (f) SEM image of o-KNbO$_3$ NWs. M: m-KNbO$_3$ NWs; O: o-KNbO$_3$ NWs.

Table 1 Physicochemical properties of *m*- and *o*-KNbO₃ NWs

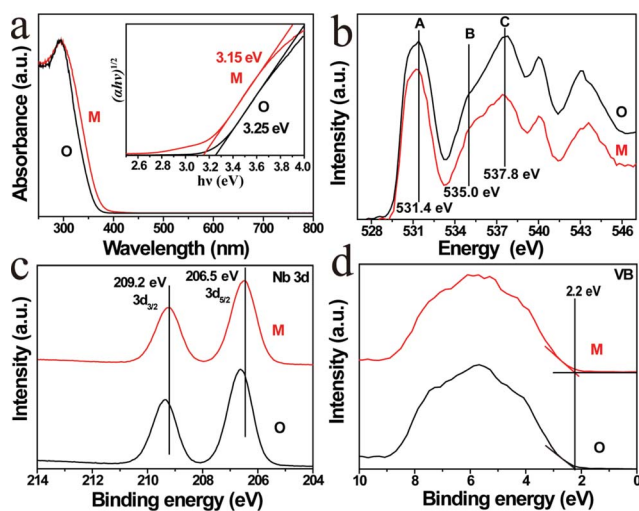| Samples	Surface area [m² g⁻¹]	Bandgap [eV]	Exposed facets	Polarization [μC cm⁻²]	Density of Nb₅c [atoms nm⁻²]	Reaction rate [×10⁻³ min⁻¹]
m-KNbO₃	4.7	3.15	{010}	20	5.90	2.04
			{001}		5.92	
			{100}		5.93	
o-KNbO₃	4.8	3.25	{010}	42	5.90	4.21
			{101}		6.14	

Fig. 2 (a) DRUV-vis spectra and corresponding plots of $(\alpha h\nu)^{1/2}$ *versus* photon energy ($h\nu$). (b) O *K*-edge XANES spectra. (c) High-resolution XPS spectra of Nb 3d core-level. (d) Valence band spectra. M: *m*-KNbO₃ NWs; O: *o*-KNbO₃ NWs.

bandgap than *m*-KNbO₃ NWs, the conduction band (CB) minimum of the *o*-KNbO₃ NWs should be raised with respect to that of *m*-KNbO₃ NWs. The above results demonstrate the intrinsic differences of the geometric structure and electronic structure between the *m*- and *o*-KNbO₃ NWs, albeit that they share similar size, crystallinity and specific surface area.

To examine the geometric structure of the *m*- and *o*-KNbO₃ NWs at an atomic level, we utilized annular-bright-field (ABF)-STEM.[49] In general, the contrast of ABF imaging depends on $Z^{1/3}$ (Z is the atomic number) and light elements like O can be directly visualized at a subangstrom resolution.[50] Therefore, the understanding of ABF imaging contrast in metal oxides is straightforward. Herein, the spots of black, dark grey and light grey correspond to NbO ($Z_{Nb} = 41$), K ($Z_K = 19$) and O ($Z_O = 8$) columns seen end-on, respectively. The representative surface structure of the *m*- and *o*-KNbO₃ NWs is revealed by profile-view imaging (Fig. 3a and b) taken along the [010] direction. Cyan, red and purple symbols denote NbO, K and O columns, respectively. According to the corresponding line profiles (Fig. 3c and d), the spacing between NbO columns (4.02 Å and 4.04 Å) fits well to *m*-KNbO₃ (001) and *o*-KNbO₃ ($\bar{1}$01), respectively. The outmost surface layer of *m*-KNbO₃ (001) and *o*-KNbO₃ ($\bar{1}$01) is NbO₂ terminated, where the exposed Nb cation (denoted as Nb₅c) is bonded to five oxygen anions. In general, the

coordinatively unsaturated surface cations often act as active sites in heterogeneous photocatalysis.[32] Additionally, neither surface relaxations nor reconstructions are observed. Other facets like {100} and {010} of *m*-KNbO₃, and {010} of *o*-KNbO₃, are also predominantly NbO₂ terminated (data not shown).

The local bulk structure of the KNbO₃ NWs is directly visualized as well. To identify the precise atomic positions from ABF images at an accuracy of several picometers and then quantitatively determine the delicate structural difference, we employed Bragg filtering and the "Find Peaks" option based on Peak Pairs Analysis.[51,52] The atomic column locations are obtained as coordinates (x, y) by fitting a two-dimensional (2D) quadratic function and calculating the maxima of the atomic column positions. The ABF imaging of the *m*- and *o*-KNbO₃ NWs viewed along different crystallographic directions with overlaid red dots obtained by Peak Pairs Analysis in Fig. 4 clearly shows the precise atomic column positions. As schematically illustrated by representative zoom-in colour-enhanced ABF images (Fig. 4), clear atomic displacements with respect to the KNbO₃ cubic structure are observed.[44] For example, the zoom-in colour-enhanced ABF images in Fig. 4a show that the NbO columns
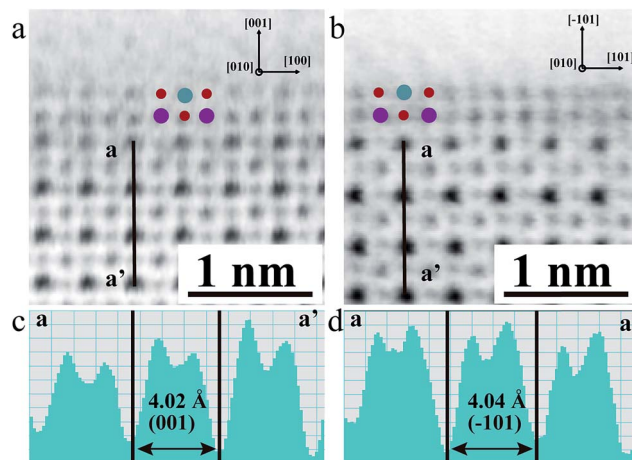

Fig. 3 Representative atomic-scale surface structure of *m*- and *o*-KNbO₃ NWs by ABF-STEM profile-view imaging. (a) *m*-KNbO₃ viewed along the [010] direction (cyan: NbO; red: O; purple: K). (b) *o*-KNbO₃ viewed along the [010] direction (cyan: NbO; red: O; purple: K). (c) Corresponding line profiles showing the image intensity as a function of the position in image (a) along a−a′. (d) Corresponding line profiles showing the image intensity as a function of the position in image (b) along a−a′.
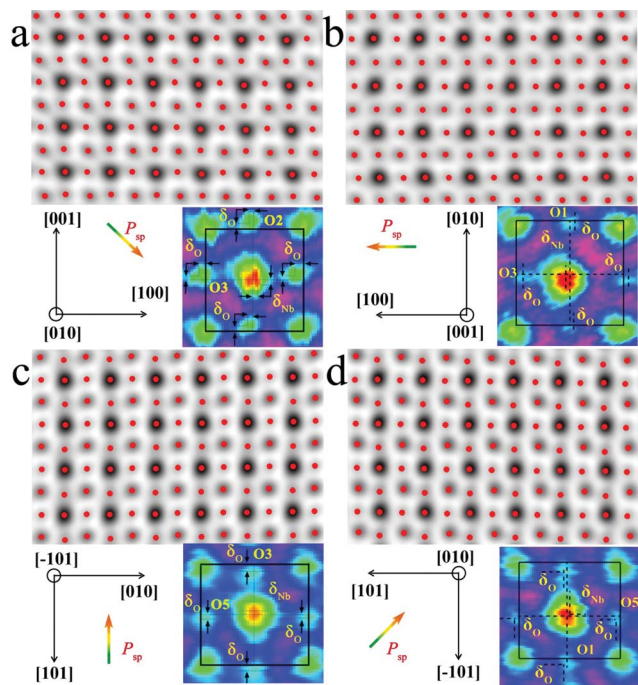
Fig. 4 Representative atomic-scale bulk structure of the m- and o-KNbO$_3$ NWs by ABF-STEM imaging. The images are overlaid with red dots that represent atomic column positions at an accuracy of several picometers obtained by Peak Pairs Analysis. Corresponding zoom-in colour-enhanced ABF images are highlighted. (a) m-KNbO$_3$ NWs viewed along the [010] direction. (b) m-KNbO$_3$ NWs viewed along the [001] direction. (c) o-KNbO$_3$ NWs viewed along the [$\bar{1}$01] direction. (d) o-KNbO$_3$ NWs viewed along the [010] direction. P_{sp} is the polarization.

shift to the lower-right and the O columns shift to the upper-left within the rectangles formed by four K columns. Table S1† displays the displacements of the Nb atoms and O atoms along different directions, denoted as δ_{Nb} and δ_O, respectively. Herein, different O atoms are numbered according to the coordinates. The atomic displacements in the m-KNbO$_3$ NWs of O1, O2, O3 and Nb1 are -0.12 ± 0.05, -0.11 ± 0.03, -0.10 ± 0.04 and 0.05 ± 0.03 Å along the [100] direction, and 0.11 ± 0.06, 0.10 ± 0.04, 0.11 ± 0.03 and -0.05 ± 0.04 Å along the [001] direction. No detectable displacements are probed for the Nb and O atoms along the [010] direction. As for the o-KNbO$_3$ NWs, the atomic displacements of O1, O3, O5 and Nb1 are 0.22 ± 0.03, 0.21 ± 0.05, 0.21 ± 0.04 and -0.15 ± 0.05 Å along the [$\bar{1}$01] direction, and 0.21 ± 0.06, 0.20 ± 0.03, 0.21 ± 0.05 and -0.14 ± 0.04 Å along the [101] direction. Additionally, no detectable displacements are observed along the [010] direction for the Nb and O atoms. The observed difference in atomic displacements for m- and o-KNbO$_3$ is due to the intrinsic structural discrepancy. The atomic displacements are corroborated by spin-polarized DFT calculations as shown in Tables S2 and S3,† which are in good agreement with the STEM measurements.

In the KNbO$_3$ unit cell, spontaneous ferroelectric polarization (denoted as P_{sp}) arises from the displacement of the positive charge center and negative charge center. K contribution to the total polarization is negligible due to the essential ionic interaction between K and O.[53] P_{sp} is calculated on the basis of

lattice parameters, atomic displacements and Born effective charges of the ions, while the Born effective charges are determined using spin-polarized DFT calculations.[44,54] The results are shown in Tables S2 and S3.† The vector of P_{sp} is pointed from the net negative to the net positive charge. As for m-KNbO$_3$, the local polarization is 20 μC cm^{-2} along the $\langle10\bar{1}\rangle$ direction. In the case of o-KNbO$_3$, the local polarization is 42 μC cm^{-2} along the $\langle001\rangle$ direction. Due to the crystal size limitations, mapping polarization domains in KNbO$_3$ NWs by STEM imaging is difficult. Nevertheless, the delicate structural variation-derived local polarization is distinct between m- and o-KNbO$_3$ NWs and expected to cause different photocatalysis.

The photoreactivity of the KNbO$_3$ NWs was assessed towards RhB degradation in water under UV light. The reaction rate constants were calculated and the results are displayed in Fig. 5a. In the absence of KNbO$_3$, RhB degradation is negligible (data not shown). Under identical experimental conditions, the o-KNbO$_3$ NWs displayed photoreactivity ($k = 4.21 \times 10^{-3}$ min^{-1}) that is about two-fold as large as that of the m-KNbO$_3$ NWs ($k = 2.04 \times 10^{-3}$ min^{-1}). The physicochemical properties of the as-prepared KNbO$_3$ NWs are summarized in Table 1. Furthermore, the photostability was examined and the results are shown in the ESI (Fig. S3–S5†). With regard to the reaction products concerning RhB degradation, such as total organic carbon (TOC), intermediate products, and inorganic mineralization species, detailed analyses along with proposed reaction pathways are given in the ESI (Tables S4, S5 and Fig. S6–S8).†

To explore the photoreactivity difference between the m- and o-KNbO$_3$ NWs, a brief overview of photocatalytic process follows. In general, semiconductor-based photocatalysis involves three steps: the photogeneration of e$^-$–h$^+$ pairs, the separation and transport of e$^-$–h$^+$, and their reaching the surface and reaction with the adsorbates. In the first step, the electronic structure, like the bandgap of a given photocatalyst, determines the light absorption and redox potentials of photo-induced charge carriers.[31] Because the o-KNbO$_3$ NWs have a greater bandgap than the m-KNbO$_3$ NWs, the o-KNbO$_3$ NWs possess a higher CB minimum than the m-KNbO$_3$ NWs and thus
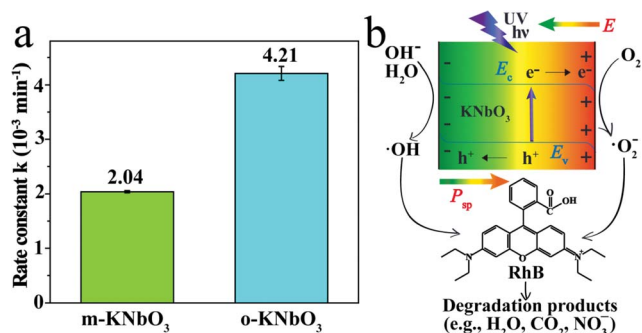

Fig. 5 (a) Photoreactivity of the m- and o-KNbO$_3$ NWs towards RhB degradation in water under UV light. (b) Representative schematic illustration of charge separation in the KNbO$_3$ NWs under UV light and associated photocatalytic degradation of RhB. E_v is the valence band edge, E_c is the conduction band edge, P_{sp} is the polarization and E is the internal electric field.

generate more strongly reductive electrons in photocatalysis.[34] The discrepancy of electronic structure is in good agreement with structural variations between *m*- and *o*-KNbO$_3$. The key issue in the second step is the charge pair recombination. Utilizing an internal electric field as a driving force is an emerging approach to suppress e$^-$–h$^+$ recombination.[18,19] Recent photocatalytic studies on the effects of an internal electric field in BaTiO$_3$,[55] ZnS,[56] AgI[4] and BiVO$_4$ [57] were only qualitatively discussed. In the present study, the magnitude of local polarization for *m*- and *o*-KNbO$_3$ is determined. The *o*-KNbO$_3$ NWs present polarization of 42 μC cm^{-2} along the ⟨001⟩ direction. As for *m*-KNbO$_3$, the polarization is 20 μC cm^{-2} along the ⟨10$\bar{1}$⟩ direction. As such, a positive charge on the surface is produced when polarization points from the bulk to the surface and *vice versa*. To compensate this bound charge, both internal screening and external screening occur.[55] For internal screening, the free charge carriers in the bulk move to the opposite charged surfaces, resulting in respective downward and upward band bending on positive and negative charged surfaces as shown in Fig. 5b. The resulting band bending further provides a driving force for the spatial separation of photo-excited electrons and holes.[19] External screening refers to the adsorption of molecules like RhB. Based on the above analysis, the *o*-KNbO$_3$ NWs exhibit more enhanced photoreactivity than the *m*-KNbO$_3$ NWs, illustrating that the greater the local polarization, the more enhanced the photoreactivity. The third step is relevant to the photocatalyst surface structure. Herein, the respective density of Nb$_{5c}$ for *m*-KNbO$_3$ NWs {010}, {001} and {100} is 5.90, 5.92 and 5.93 atoms nm^{-2}, very similar to 5.90 and 6.14 atoms nm^{-2} for {010} and {101} of the *o*-KNbO$_3$ NWs. Therefore, in this work the surface structure is most likely not a leading factor in causing the distinct photocatalytic performance. Considering that the *o*-KNbO$_3$ NWs are able to generate more strongly reductive electrons than their *m*-KNbO$_3$ counterparts under UV light, we can conclude that both ferroelectric polarization and electronic structure synergistically dictate the photocatalytic performance. Unlike previous studies that emphasized the effects of exposed facets[34–38] in photocatalysis, our results indicate that ferroelectric polarization dictates the photoreactivity by driving e$^-$ and h$^+$ to the photocatalyst surface to trigger the photocatalytic reaction, albeit the facets of the *m*- and *o*-KNbO$_3$ NWs expose comparable surface low-coordinate Nb density. This is, therefore, a unique route for directing the transport of photo-excited charge carriers and enhancing the photoreactivity.

Conclusions

In summary, with a combination of advanced ABF-STEM imaging and DFT calculations, we directly probed the atomic surface structure, measured delicate atomic displacements at an accuracy of several picometers, and quantified associated local polarization in single-crystalline *m*- and *o*-KNbO$_3$ NWs with comparable size, crystallinity and specific surface area. Orthorhombic KNbO$_3$ nanowires displayed RhB photodegradation about two-fold as large as their monoclinic counterparts and the underlying mechanism can be rationalized as a novel synergy of delicate atomic structural variation-derived ferroelectric polarization and electronic structure. Additionally, RhB degradation pathways are proposed, with an emphasis on *N*-deethylation and conjugated structure cleavage. Our results are potentially applicable to a range of perovskite ferroelectric materials functional in light-mediated environment remediation and energy production.

Acknowledgements

Notes and references

1 A. Fujishima and K. Honda, *Nature*, 1972, **238**, 37–38.
2 C. C. Chen, W. H. Ma and J. C. Zhao, *Chem. Soc. Rev.*, 2010, **39**, 4206–4219.
3 R. Asahi, T. Morikawa, T. Ohwaki, K. Aoki and Y. Taga, *Science*, 2001, **293**, 269–271.
4 Q. Kuang, X. L. Zheng and S. H. Yang, *Chem.–Eur. J.*, 2014, **20**, 2637–2645.
5 M. R. Hoffmann, S. T. Martin, W. Y. Choi and D. W. Bahnemann, *Chem. Rev.*, 1995, **95**, 69–96.
6 X. J. Lang, W. H. Ma, C. C. Chen, H. W. Ji and J. C. Zhao, *Acc. Chem. Res.*, 2014, **47**, 355–363.
7 X. M. Zhou, G. Liu, J. G. Yu and W. H. Fan, *J. Mater. Chem.*, 2012, **22**, 21337–21354.
8 A. Tanaka, K. Hashimoto and H. Kominami, *J. Am. Chem. Soc.*, 2014, **136**, 586–589.
9 A. Kudo and Y. Miseki, *Chem. Soc. Rev.*, 2009, **38**, 253–278.
10 K. Maeda, K. Teramura, D. L. Lu, T. Takata, N. Saito, Y. Inoue and K. Domen, *Nature*, 2006, **440**, 295.
11 X. B. Chen, S. H. Shen, L. J. Guo and S. S. Mao, *Chem. Rev.*, 2010, **110**, 6503–6570.
12 F. E. Osterloh, *Chem. Soc. Rev.*, 2013, **42**, 2294–2320.
13 T. Hisatomi, J. Kubota and K. Domen, *Chem. Soc. Rev.*, 2014, **43**, 7520–7535.
14 S. Li, J. M. Zhang, M. G. Kibria, Z. T. Mi, M. Chaker, D. L. Ma, R. Nechache and F. Rosei, *Chem. Commun.*, 2013, **49**, 5856–5858.
15 A. Hagfeldt and M. Grätzel, *Chem. Rev.*, 1995, **95**, 49–68.
16 Y. Q. Qu and X. F. Duan, *Chem. Soc. Rev.*, 2013, **42**, 2568–2580.
17 R. G. Li, F. X. Zhang, D. G. Wang, J. X. Yang, M. R. Li, J. Zhu, X. Zhou, H. X. Han and C. Li, *Nat. Commun.*, 2013, **4**, 1432.
18 C. R. Bowen, H. A. Kim, P. M. Weaver and S. Dunn, *Energy Environ. Sci.*, 2014, **7**, 25–44.
19 L. Li, P. A. Salvador and G. S. Rohrer, *Nanoscale*, 2014, **6**, 24–42.

20 C. Hengky, X. Moya, N. D. Mathur and S. Dunn, *RSC Adv.*, 2012, **2**, 11843–11849.

21 M. Stock and S. Dunn, *J. Phys. Chem. C*, 2012, **116**, 20854–20859.

22 S. Park, C. W. Lee, M. G. Kang, S. Kim, H. J. Kim, J. E. Kwon, S. Y. Park, C. Y. Kang, K. S. Hong and K. T. Nam, *Phys. Chem. Chem. Phys.*, 2014, **16**, 10408–10413.

23 Z. Z. Lou, B. B. Huang, Z. Y. Wang, X. C. Ma, R. Zhang, X. Y. Zhang, X. Y. Qin, Y. Dai and M. H. Whangbo, *Chem. Mater.*, 2014, **26**, 3873–3875.

24 X. Y. Fan, L. Zang, M. Zhang, H. S. Qiu, Z. Wang, J. Yin, H. Z. Jia, S. L. Pan and C. Y. Wang, *Chem. Mater.*, 2014, **26**, 3169–3174.

25 C. T. Campbell, *Top. Catal.*, 2013, **56**, 1273–1276.

26 V. Subramanian, E. E. Wolf and P. V. Kamat, *J. Am. Chem. Soc.*, 2004, **126**, 4943–4950.

27 S. Chen, J. J. Duan, M. Jaroniec and S. Z. Qiao, *Adv. Mater.*, 2014, **26**, 2925–2930.

28 Y. M. Li and G. A. Somorjai, *Nano Lett.*, 2010, **10**, 2289–2295.

29 H. G. Yang, C. H. Sun, S. Z. Qiao, J. Zou, G. Liu, S. C. Smith, H. M. Cheng and G. Q. Lu, *Nature*, 2008, **453**, 638–641.

30 Y. D. Yin and D. Talapin, *Chem. Soc. Rev.*, 2013, **42**, 2484–2487.

31 H. Tong, S. X. Ouyang, Y. P. Bi, N. Umezawa, M. Oshikiri and J. H. Ye, *Adv. Mater.*, 2012, **24**, 229–251.

32 X. M. Zhou, J. Y. Lan, G. Liu, K. Deng, Y. L. Yang, G. J. Nie, J. G. Yu and L. J. Zhi, *Angew. Chem., Int. Ed.*, 2012, **51**, 178–182.

33 X. M. Zhou, Q. L. Xu, W. Y. Lei, T. T. Zhang, X. Y. Qi, G. Liu, K. Deng and J. G. Yu, *Small*, 2014, **10**, 674–679.

34 J. Pan, G. Liu, G. Q. Lu and H. M. Cheng, *Angew. Chem., Int. Ed.*, 2011, **50**, 2133–2137.

35 A. Selloni, *Nat. Mater.*, 2008, **7**, 613–615.

36 Y. P. Bi, S. X. Ouyang, N. Umezawa, J. Y. Cao and J. H. Ye, *J. Am. Chem. Soc.*, 2011, **133**, 6490–6492.

37 Z. B. Jiao, Y. Zhang, H. C. Yu, G. X. Lu, J. H. Ye and Y. P. Bi, *Chem. Commun.*, 2013, **49**, 636–638.

38 D. J. Martin, N. Umezawa, X. W. Chen, J. H. Ye and J. W. Tang, *Energy Environ. Sci.*, 2013, **6**, 3380–3386.

39 T. T. Zhang, K. Zhao, J. G. Yu, J. Jin, Y. Qi, H. Q. Li, X. J. Hou and G. Liu, *Nanoscale*, 2013, **5**, 8375–8383.

40 M. A. Peña and J. L. G. Fierro, *Chem. Rev.*, 2001, **101**, 1981–2017.

41 L. Vayssieres, C. Sathe, S. M. Butorin, D. K. Shuh, J. Nordgren and J. H. Guo, *Adv. Mater.*, 2007, **17**, 2320–2323.

42 S. K. Mohapatra, S. E. John, S. Banerjee and M. Misra, *Chem. Mater.*, 2009, **21**, 3048–3055.

43 K. W. Urban, *Science*, 2008, **321**, 506–510.

44 C. L. Jia, S. B. Mi, K. Urban, I. Vrejoiu, M. Alexe and D. Hesse, *Nat. Mater.*, 2008, **7**, 57–61.

45 S. Kim, J. H. Lee, J. Lee, S. W. Kim, M. H. Kim, S. Park, H. Chung, Y. I. Kim and W. Kim, *J. Am. Chem. Soc.*, 2013, **135**, 6–9.

46 J. Y. Lan, X. M. Zhou, G. Liu, J. G. Yu, J. C. Zhang, L. J. Zhi and G. J. Nie, *Nanoscale*, 2011, **3**, 5161–5167.

47 Q. P. Ding, Y. P. Yuan, X. Xiong, R. P. Li, H. B. Huang, Z. S. Li, T. Yu, Z. G. Zou and S. G. Yang, *J. Phys. Chem. C*, 2008, **112**, 18846–18848.

48 L. Douillard, F. Jollet, C. Bellin, M. Gautier and J. P. Duraud, *J. Phys.: Condens. Matter*, 1994, **6**, 5039–5052.

49 S. J. Pennycook and D. E. Jesson, *Phys. Rev. Lett.*, 1990, **64**, 938–941.

50 Y. Sun, L. Zhao, H. L. Pan, X. Lu, L. Gu, Y. S. Hu, H. Li, M. Armand, Y. Ikuhara, L. Q. Chen and X. J. Huang, *Nat. Commun.*, 2013, **4**, 1870.

51 P. L. Galindo, S. Kret, A. M. Sanchez, J. Y. Laval, A. Yáñez, J. Pizarro, E. Guerrero, T. Ben and S. I. Molina, *Ultramicroscopy*, 2007, **107**, 1186–1193.

52 P. Galindo, J. Pizarro, S. Molina and K. Ishizuka, *Microsc. Anal.*, 2009, **23**, 23–25.

53 J. Shi, I. Grinberg, X. L. Wang and A. M. Rappe, *Phys. Rev. B: Condens. Matter Mater. Phys.*, 2014, **89**, 094105.

54 L. Y. Li, Z. F. Gan, M. R. McCartney, H. S. Liang, H. B. Yu, W. J. Yin, Y. F. Yan, Y. H. Gao, J. B. Wang and D. J. Smith, *Adv. Mater.*, 2014, **26**, 1052–1057.

55 Y. F. Cui, J. Briscoe and S. Dunn, *Chem. Mater.*, 2013, **25**, 4215–4223.

56 Y. P. Hong, J. Zhang, X. Wang, Y. J. Wang, Z. Lin, J. G. Yu and F. Huang, *Nanoscale*, 2012, **4**, 2859–2862.

57 R. Munprom, P. A. Salvador and G. S. Rohrer, *Chem. Mater.*, 2014, **26**, 2774–2776.